UNDERSTANDING AND CONTROLLING THE OXIDATION BEHAVIOR OF BINARY REFRACTORY ALLOYS

Lauren Bowling, University of Virigina

Elizabeth Opila, University of Virgina

Abstract

This work focuses on the formation and protective capabilities of the $TiNb_2O_7$ and $CrTaO_4$ complex refractory oxides. Binary Ti-Nb alloys were oxidized to investigate the compositional limits of $TiNb_2O_7$ formation. The resulting thermally grown oxide scales were characterized via micro-area x-ray diffraction, scanning electron microscopy, and energy dispersive spectroscopy. A critical Nb concentration that controls oxidation resistance and $TiNb_2O_7$ growth within the binary system was observed. Determination of the intrinsic oxygen diffusion coefficients of $CrTaO_4$ were measured to quantify the protectiveness of $CrTaO_4$. Measurements were achieved through the combination of tracer diffusion experiments (using ^{18}O), time-of-flight secondary ion mass spectroscopy, and modeling Fick's second law. Preliminary results indicate that $CrTaO_4$ could be used as a protective oxide.

1. Introduction

The development of next-generation land-based gas turbines or aeroengines is driven by the need for improved engine efficiency[1,2]. This improved efficiency is achieved through raising the combustion temperature and therefore, through raising the temperature of the hot-section structures within the engine. The temperature is currently limited by the Ni-base superalloys employed as structural components, as they have a maximum operational temperature of approximately 1100˚C [2,3]. Above 1100˚C, the γ' phase in the γ- γ' microstructure coarsens, leading to precipitate dissolution, and henceforth, incipient melting[4,5]. Design parameters of the next-generation engines call for materials that can not only survive at temperatures above 1300˚C, but also maintain load bearing capability[6]. Therefore, replacement materials are needed to break the temperature barrier imposed by Ni-base superalloys.

Of the possible candidates, refractory alloys are considered due to their high melting points (>2000˚C)[7]. In the 1960s, the high melting points of refractory alloys gained attention for use in processes with aerothermal heating, such as high-velocity flight or re-entry vehicles[8]. From this research effort, the current commercially available Nb-alloy, C103 (Nb-10Hf-1Ti wt%), was developed, and has since been used in rocket nozzles[9] and as thrust augmenter flaps[10]. However, refractory alloy use within combustion system-like environments is limited due to their poor oxidation resistance. For example, an uncoated C103 sample fully oxidized in lab air at 1350°C after 24 h (Figure 1). This is problematic, as the service life required for some combustion engine components can range from tens to thousands of hours, depending on the specific application[5]. Therefore, the catastrophic oxidation of C103 demonstrates the undeniable need to develop refractory alloys with improved, intrinsic, oxidation resistance.

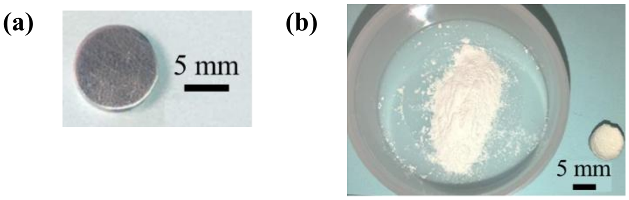

Figure 1. *(a) C103 coupon prior to exposure and (b) the completely oxidized C103 coupon after exposure to lab air at 1350°C for 24 h. Figure adapted from*[11].

The poor oxidation resistance of refractory alloys is due to the non-protective binary metal oxides that form (i.e., A_xO_y), as these oxides can allow for fast oxygen diffusion, promote crack propagation and growth, and form gaseous oxides[12]. Therefore, binary refractory oxides cannot be the main thermally grown oxide (TGO) of a refractory alloy for the alloy to have inherent oxidation resistance. Rather, it has been proposed that the presence of some *complex* refractory oxides (i.e., ternary oxides $A_xB_yO_z$) can improve the oxidation resistance of these alloys[13–20].

Numerous complex refractory oxides have been identified in the literature as potential protective oxides, including $Hf_6Ta_2O_{17}$[13,14], $Zr_6Nb_2O_{17}$[15], $TiNb_2O_7$[16], $ZrNb_2O_7$[17], $CrTaO_4$[18–20], and $CrNbO_4$[18]. In most studies, this identification originated from the observation of reduced alloy oxidation coupled with the presence of the corresponding complex oxide within the TGO. Therefore, this work focuses on developing an understanding of the protectiveness of individual complex refractory oxides.

To accomplish this, this work is divided into two tasks and focuses on $TiNb_2O_7$ and $CrTaO_4$. In the first task, binary Ti-Nb alloys were studied to understand the compositional effects of varying Ti/Nb ratios on the formation of $TiNb_2O_7$. The second task focuses on quantifying the protectiveness of $CrTaO_4$ through measuring the intrinsic oxygen diffusion coefficients.

2. Methods and Materials

2.1 Thermal Growth of $TiNb_2O_7$

Five single-phased Ti-Nb alloys were prepared via arc-melting (nominal compositions in Table 1). The chamber was purged and backfilled with Ar three times and a final pressure of approximately 0.99 atm was used for melting. Alloys were melted and flipped five times to ensure full melting and homogenization, a Ti-getter was melted each time before and after the alloys to scrub any residual oxygen from the environment. As-cast alloys were homogenized in Ar at 1250°C for 24 h via encapsulation in fused quartz tubes. For homogenization, samples were purged and backfilled with Ar three times prior to a final backfill of approximately 0.99 atm of Ar. Ti-sponge was included within the capsule as a getter for any remaining oxygen within the system.

Table 1. *Nominal Composition of Investigated Ti-Nb Alloys*

	Alloy 1	Alloy 2	Alloy 3	Alloy 4	Alloy 5
Ti (at%)	80	66	50	40	20
Nb (at%)	20	34	50	60	80

2.1.1 Oxidation Exposures

Oxidation exposures were conducted in a horizontal tube furnace (CM Furnaces, Bloomfield, NJ) at 1050°C for 20 h in a flowing 1% O_2 – Ar atmosphere (100 sccm); such conditions are common within literature[21]. All sample faces were polished to an 800-grit finish with SiC prior to oxidation.

The specific mass change of each sample was used to quantify the degree of sample oxidation and was calculated via normalizing the mass change by sample surface area. Mass change was determined from pre- and post-exposure weights. Sample surface area was calculated using the face area, initial thickness, and perimeter of the sample; face area and perimeter were measured via thresholding in ImageJ[22]. Relative metal recession measurements were also calculated and taken as the thickness lost (initial alloy thickness – post-oxidation alloy thickness) normalized by the initial alloy thickness (post-oxidation alloy thickness was measured from cross-sectional SEM images in ImageJ[22]). Error bars of the recession measurements were determined through the propagation of uncertainty method.

2.1.2 X-Ray Diffraction

Oxidized samples were characterized via micro-area x-ray diffraction (μ-XRD) to confirm phases present and to conduct quantitative phase analysis through Rietveld refinement in GSAS-ii[23]. Micro-area XRD can collect high-intensity scans from 0.5 mm^2 or 0.2 mm^2 sized areas (roughly 0.5 mm or 0.2 mm by 1 mm), allowing specific regions within an oxide scale to be studied. θ-2θ scans were collected on a Rigaku SmartLab X-ray diffractometer and 0.5 mm^2 cross-beam optics were used on plan-view samples to identify the thermally grown oxides. HighScore+ [24] was used for phase identification.

Rietveld refinement was used for phase volume fraction quantification, a powder-LaB_6 standard was used to determine instrument parameters in GSAS-ii[23,25]. ICDD PDF-5+ [26] was used to generate .cif files for each phase; $TiNb_2O_7$ files lacked the crystallographic parameters needed for Rietveld refinement, therefore, lattice parameters and atomic positions were taken from[27]. The volume fraction (v_f) of each oxide within a TGO was calculated from the GSAS-ii reported weight fraction and density of each oxide.

2.1.3 Scanning Electron Microscopy

Scanning electron microscopy (SEM) was employed for phase distribution information (FEI Quanta 650 SEM) and was coupled with energy dispersive spectroscopy (EDS) for elemental information (Oxford Silicon drift detector). All samples were polished to a 0.25 µm surface finish and sputter coated with a 16 nm thick AuPd coating.

2.1.4 Thermodynamic Predictions

Gaskell[28] proposed a model that enables the prediction of the constitution of an oxide scale based on the composition of the base alloy and the assumption that the oxides and metals are in respective ideal solutions. This approach has previously been applied to the Hf-Zr-O system[29]. The calculation is governed by an equilibrium reaction between the oxides of interest and metals within the base alloy. As $TiNb_2O_7$ only exists as a line compound[30], the TiO_2 + $TiNb_2O_7$ phase region was modeled. Equation (1) was taken as the equilibrium reaction, where the more stable oxide, TiO_2, was a product and the metals, Ti and Nb, were placed on the reactants or products side according to mass balance.

From (1), the Gibbs free energy of the reaction (ΔG_{rxn}) was calculated using the educational FactSage 8.4 software, the TiO_2 thermodynamic data in the FactPS database[31], and $TiNb_2O_7$ thermodynamic data from the Thermo-Calc TCOX11 v11.1 database[32]. From ΔG_{rxn}, the reaction product, K, can be calculated per (2); K can also be calculated from the equilibrium molar fractions of each species (denoted with an 'x' in (2)). As the oxides are assumed to be in an ideal solution with each other, their molar fractions must sum to one, allowing (2) to calculate the molar fraction of $TiNb_2O_7$ as a function of alloy composition.

$$\frac{5}{14}\mathrm{Ti} + \frac{1}{7}\mathrm{TiNb_2O_7} = \frac{1}{2}\mathrm{TiO_2} + \frac{2}{7}\mathrm{Nb} \qquad (1)$$

$$K = e^{-\frac{\Delta G_{rxn}}{R \cdot T}} = \frac{[xTiO_2]^{\frac{1}{2}} \cdot [xNb]^{\frac{2}{7}}}{[xTiNb_2O_7]^{\frac{1}{7}} \cdot [xTi]^{\frac{5}{14}}} = \frac{[1 - xTiNb_2O_7]^{\frac{1}{2}} \cdot [xNb]^{\frac{2}{7}}}{[xTiNb_2O_7]^{\frac{1}{7}} \cdot [xTi]^{\frac{5}{14}}} \qquad (2)$$

Results for the TiO_2 + $TiNb_2O_7$ system at 1050°C are shown in Figure 2, wherein $TiNb_2O_7$ is predicted to never form at 1050°C across the Ti-Nb compositional range. Per the phase diagram[30], this result is unexpected as TiO_2 and $TiNb_2O_7$ can exist in equilibrium together. These modeling results also differ from the experimentally observed results, which are discussed in future sections; this indicates that the growth of $TiNb_2O_7$ is either significantly influenced by kinetics, that the $TiNb_2O_7$ data used within the calculation requires improvement, or that the model does not accurately describe the system.

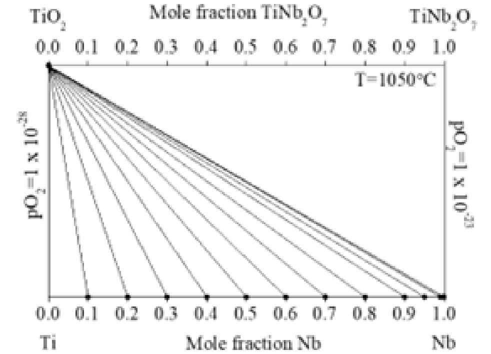

Figure 2. *Compositional balance diagram of the Ti-Nb-TiO_2-$TiNb_2O_7$ system. No $TiNb_2O_7$ was predicted to form across the Ti-Nb compositional space.*

2.2 Oxygen Diffusion Coefficients of $CrTaO_4$

A $CrTaO_4$ puck (20 mm diameter x 2 mm thick) was synthesized via spark plasma sintering (SPS) from an equimolar mixture of the binary oxides (e.g., Cr_2O_3 (Thermo Fisher Scientific) and Ta_2O_5 (ABCR, Karlsruhe)), which was ball milled with ZrO_2 media for approximately 24 h prior to SPS. Powders were sintered at 1500°C and 65 MPa for 15 min and the resulting puck was measured to be 99% dense per the Archimedes method[33]. XRD and SEM were conducted on the as-sintered puck to ensure single phase and gain grain size information. $CrTaO_4$ samples were polished to a 0.05 µm finish prior to encapsulation.

2.2.1 Tracer Diffusion

Tracer diffusion experiments consist of a double oxygen exposure, where the first exposure is in an $^{16}O_2$ environment and held for a significantly longer time than the second exposure. The second exposure is conducted in an $^{18}O_2$ environment for ^{18}O to exchange with the ^{16}O in the oxide. The longer $^{16}O_2$ exposure ensures a constant chemical potential of ^{16}O throughout the sample such that an intrinsic diffusion coefficient can be accurately measured. Exposure times and temperatures are in Table 2.

Table 2. *$CrTaO_4$ Tracer Diffusion Times and Temperatures*

Exposure Temperature (°C)	$^{16}O_2$ Time (h)	$^{18}O_2$ Time (h)
1100	240	36
1200	168	16.8

Samples were encapsulated in fused quartz tubes via a system schematically shown in Figure 3. For the $^{16}O_2$ environment, the sample was pumped down to < 20 mT and backfilled to 0.68 atm with $^{16}O_2$ to ensure that the capsule would not cave-in from external pressure. The system was not flushed with Ar prior to backfilling, as $^{16}O_2$ is naturally abundant in any residual air within the capsule. Capsules were then loaded into a box furnace (CM Furnaces, Bloomfield, NJ) at-temperature and water quenched immediately after the exposure was complete. The process of encapsulating in an $^{18}O_2$ environment follows the same steps as the $^{16}O_2$ process, except that the system is purged and flushed with Ar three times prior to the final $^{18}O_2$ backfill; 0.68 atm of $^{18}O_2$ was used.

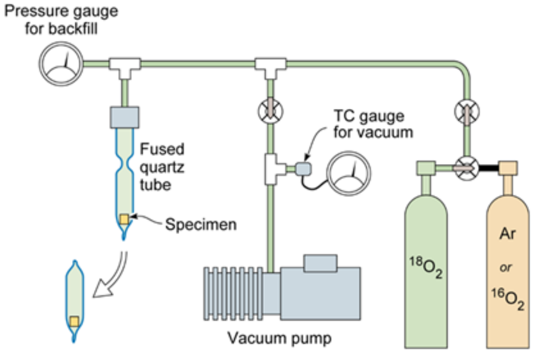

Figure 3. *Schematic of the encapsulation system used for obtaining $^{16}O_2$ and $^{18}O_2$ exposure environments.*

2.2.2 Time-of-Flight Secondary Ion Mass Spectroscopy

Time-of-flight secondary ion mass spectroscopy (ToF-SIMS) was employed to measure the ^{18}O fraction depth profile within samples. ToF-SIMS was conducted at North Carolina State University, where the instrument is equipped with a Cs ion gun for sputtering and a Bi ion gun for exciting the sample ions. The concentration of secondary ions (i.e., those emitted from the sample by the Bi-gun) are captured by a detector, where the ions are sorted by mass and charge via their time-of-flight from the sample to the detector; this allows for differentiation between the oxygen isotopes. Sputter time is converted to sputter depth by measuring the crater depth, post-ToF-SIMS, via optical profilometry (Zygo NewView 7300) and assuming a constant sputtering rate. Ionic compounds of the same formula and cation, with both ^{18}O and ^{16}O anions, were used to calculate the ^{18}O fraction profile ($c(x,t)$). This ^{18}O profile is then fit to the semi-infinite solution of Fick's second law (referred to as the bulk solution, (3) [34]), with a surface exchange limited boundary condition $D_b \left(\frac{dc}{dx}\right)_{x=0} = k_s(c_g - c_s)$, where c_s is the fraction of ^{18}O at the sample surface. The ^{18}O fraction is also adjusted in (3) to account for the natural abundance of ^{18}O (c_0 = 0.2%, 0.002) and purity of the encapsulating $^{18}O_2$ gas (c_g = 97%, 0.97). Ultimately, D_b, the intrinsic oxygen self-diffusion coefficient, and k_s, the oxygen tracer surface exchange coefficient, are solved for when fitting (3) to the ^{18}O fraction depth profile. The MATLAB app *TraceX* [35] was used to fit the bulk solution to the ^{18}O profile.

$$c'(x,t) = \frac{c\,(x,t) - c_0}{c_g - c_0} = erfc\left(\frac{x}{2\sqrt{D_b t}}\right) - \exp\left(\frac{k_s x}{D_b} + \frac{k_s^2 t}{D_b}\right) erfc\left(\frac{x}{2\sqrt{D_b t}} + k_s\sqrt{\frac{t}{D_b}}\right) \tag{3}$$

3. Results

3.1 Thermal Growth of $TiNb_2O_7$

3.1.1 Oxidation Results

Specific mass change of the alloys was observed to increase with Nb content until Ti-60Nb, which had a maximum value of 71 mg/cm^2, where then oxidation decreased with Ti-80Nb (40 mg/cm^2); the Ti-20Nb alloy oxidized the least (33 mg/cm^2) (Figure 4). The same trend was observed for the relative metal recession measurements. Error bars of the recession measurements appear relatively large due to some samples having a large range of initial thickness measurements from slight beveling from prepping sample faces for oxidation. The beveling did not appear to affect the thickness of the thermally grown oxide scale or metal recession (i.e., the TGOs had uniform thickness).

3.1.2 X-Ray Diffraction Results

Micro-area XRD revealed that the thermally grown oxide scales of each alloy were two-phased. For all alloys except Ti-80Nb, TiO_2 and $TiNb_2O_7$ were present. $TiNb_2O_7$ and $Ti_2Nb_{10}O_{29}$ were present in the scale of Ti-80Nb. These results disagree with those of the thermodynamic modeling (Figure 2), where $TiNb_2O_7$ was not predicted to form.

Rietveld refinements were finalized when the GSAS-ii reported weighted profile R-factor (Rwp%) errors were less than 10% and when there was good visual agreement between predicted and measured spectra. The maximum amount of $TiNb_2O_7$ within an oxide scale (v_f = 0.75) corresponded to the sample that oxidized the most, Ti-60Nb. Similarly, the alloy with the least amount of $TiNb_2O_7$ (v_f = 0.11), Ti-20Nb, had the lowest specific mass change and metal recession. Volume fraction of $TiNb_2O_7$ was found to trend with specific mass change and relative metal recession, in which $TiNb_2O_7$ volume fraction increased until Ti-60Nb, where after, it decreased (Figure 4).

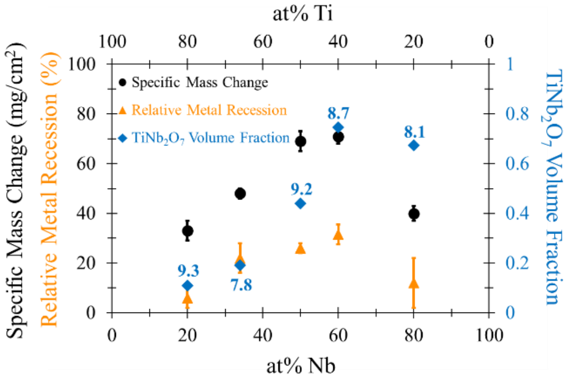

Figure 4. *Specific mass change, relative metal recession, and $TiNb_2O_7$ volume fraction trends with alloy composition. Oxidation and $TiNb_2O_7$ content increased until Ti-60Nb, beyond which, they both decreased. GSAS-ii Rwp% values are included for each alloy.*

3.1.3 Scanning Electron Microscopy Results

Cross-sectional SEM images revealed that each scale was two-phased, as informed by μ-XRD, and contained some porosity. Across the TiO_2 + $TiNb_2O_7$ containing scales, three layers were observed: (i) a thin outer layer at the gas/oxide interface, (ii) the main oxide layer, and (iii) a thin inner layer at the alloy/oxide interface (Figure 5).

The main oxide layer was composed of an inhomogeneous distribution of oxides that appeared to grow around each other rather than in a layered structure. EDS identified Ti-rich and Nb-rich regions in the oxide scale and that the oxygen content was relatively constant across the scale; this gave confidence in confirming that the dark grey oxide corresponded to TiO_2 and the light grey one to $TiNb_2O_7$ (Figure 5).

The remaining alloy material in all tested compositions was also found to be two-phased post-oxidation and per EDS, there existed Ti- and Nb-rich phases (Figure 5); μ-XRD was conducted and confirmed the presence of an hcp and bcc phase in Ti-34Nb. EDS also informed that the Ti-34Nb alloy contained a total of approximately 33 at% O across both phases, where the darker phase had at least 50 at% Ti and the lighter phase had about 25 at% Nb. It is expected that the darker phase is a Ti-O hcp phase, and the lighter phase is bcc.

As Ti-80Nb thermally grew a $TiNb_2O_7$ + $Ti_2Nb_{10}O_{29}$ scale, it demonstrated a different oxide layering scheme than the other alloys. No distinct layer existed at the gas/oxide interface, and a thick single-phase layer was present at the alloy/oxide interface. The main layer of inhomogeneously distributed oxide exhibited three distinct levels of porosity and the contrast between $TiNb_2O_7$ and $Ti_2Nb_{10}O_{29}$ decreased with increased pO_2. With respect to the remaining Ti-80Nb alloy material post-oxidation, it was also two-phased like the other alloys, but demonstrated a significantly more refined microstructure.

3.2 Oxygen Diffusion Coefficients of $CrTaO_4$

3.2.1 Tracer Diffusion Results

The 1200°C ^{18}O profile for $CrTaO_4$ is in Figure 6. The data used to fit the bulk solution with *TraceX* [35] was limited for both samples, as the diffusion distance was approximately 0.2 and 0.3 μm for 1100°C and 1200°C, respectively. Using data from deeper within the profiles resulted in poor fits (grain boundary data is identified in Figure 6). Additionally, the ^{18}O concentration near the surface of the samples was ignored due to the presence of surface containments (i.e., C, Si, Al, or Ca). Only the bulk data in which Cr and/or Ta were the dominant cations was used within the bulk model; such data is identified in Figure 6. From this, the intrinsic oxygen diffusion coefficients were not found to significantly differ between the two temperatures (Table 3).

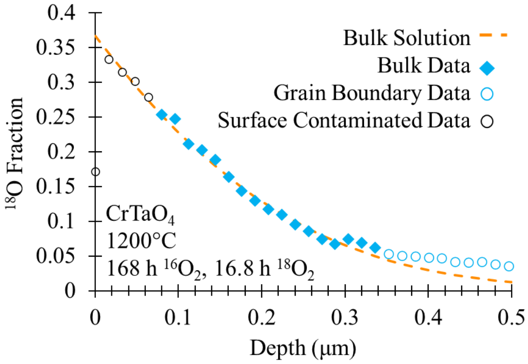

Figure 6. *The measured 1200°C $CrTaO_4$ ^{18}O profile; demonstrating a short diffusion depth and a measured profile tail higher than the bulk model, indicating the influence of grain boundary diffusion. Surface contaminated data is labeled.*

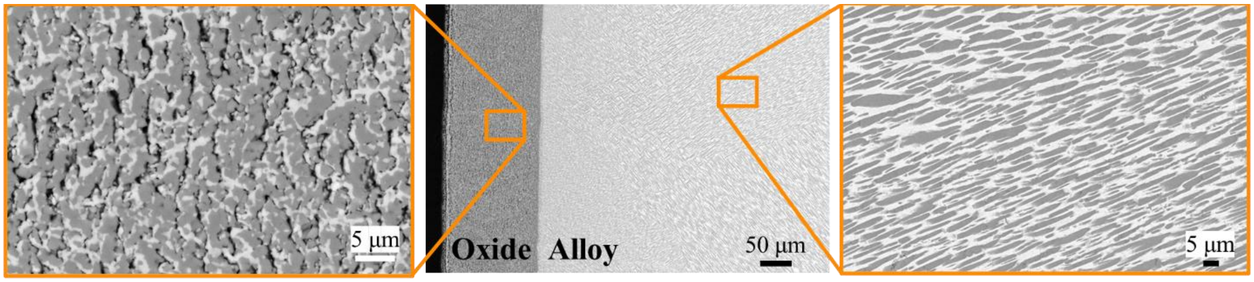

Figure 5. *Micrograph of oxidized Ti-20Nb. (Left) is an inset of the main TGO layer, which was two-phased and porous; pores are black, $TiNb_2O_7$ is light grey, and TiO_2 is dark grey. (Right) is an inset of the remaining Ti-20Nb alloy, phase separated into Ti-rich (grey) and Nb-rich (white) phases.*

Table 3. *TraceX Fit D_b and k_s Terms for 1100°C and 1200°C*

Temperature (°C)	*TraceX* Fit D_b (cm^2/s)	*TraceX* Fit k_s (cm/s)
1100	3.2×10^{-15}	3.1×10^{-11}
1200	5.5×10^{-15}	5.0×10^{-9}

4. Discussion

4.1 Thermal Growth of $TiNb_2O_7$

4.1.1 Oxidation Trends

The oxidation exposures revealed that the extent of alloy oxidation increased with increased Nb content and $TiNb_2O_7$ volume fraction until Ti-60Nb, beyond which both measurements decreased. This oxidation trend informs that a critical Nb content exists within the Ti-Nb binary alloy system, where sample oxidation increases until this critical Nb amount, and decreases when the alloyed Nb content exceeds this concentration. The exact critical composition was not determined, but is speculated to be Ti-67Nb to match the Ti:Nb ratio in $TiNb_2O_7$.

This oxidation trend also suggests that a TGO comprised of only Ti-Nb-O complex oxides (e.g., $TiNb_2O_7$ + $Ti_2Nb_{10}O_{29}$ in Ti-80Nb) is potentially more protective than a TiO_2 + $TiNb_2O_7$ scale, even when a majority of the scale consists of $TiNb_2O_7$ (Ti-60Nb). This result suggests that the Ti-Nb-O complex oxide scale behaves more like a single, continuous layer of oxide (i.e., a characteristic of protective oxide scales), as it has less porosity and improved adhesion to the alloy compared to the TiO_2 + $TiNb_2O_7$ scales.

4.1.2 Proposed Oxidation Mechanism

Ogawa et al.[36] also observed an inhomogeneous TGO distribution of TiO_2 + $TiNb_2O_7$ in Ti-Nb binary alloy TGO scales (ranging from 1.5 – 26 at% Nb) and phase separation of the base alloy in post-oxidation characterization; samples were exposed at 1000°C in lab air for 1 h. It was noted that the alloy microstructure appeared to continue into the oxide scale, and this was also observed for all TiO_2 + $TiNb_2O_7$ TGOs in this study; Figure 7 demonstrates this for Ti-20Nb at the alloy/oxide interface. Ogawa et al. also observed an increased growth rate of TiO_2 + $TiNb_2O_7$ TGOs with increased Nb content[36]. From the results presented here, it is assumed that the faster growth rate was due to increased $TiNb_2O_7$ content. From the measured growth rate, Ogawa et al. determined the oxide scale activation energy to be that of Ti or Nb diffusion in Ti-Nb alloys, indicating that the rate determining step for Ti-Nb oxidation is metallic element diffusion[36]. However, it should be noted that the activation energy for Ti or Nb in Ti-Nb alloys is heavily dependent on alloy composition and Ogawa et al. compared the measured activation energy to a literature value not representative of the tested alloy[37,38].

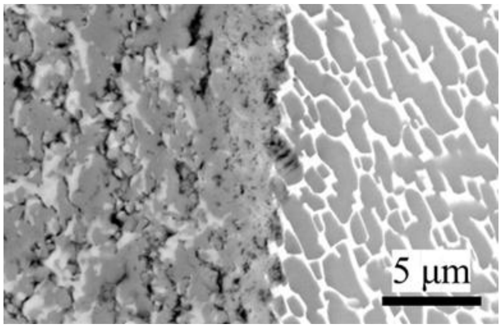

Figure 7. *Micrograph of the Ti-20Nb alloy/oxide interface, demonstrating the continuity of the alloy microstructure into the oxide scale.*

In a later study, Fujiwara and Ogawa[39] proposed a mechanism for Ti-Nb oxidation as follows: (i) the alloy oxidizes and phase separates into hcp + bcc, (ii) hcp phase transforms to TiO_2, where when Nb exceeds its solubility (~13 at%), (iii) Nb precipitates to form $TiNb_2O_7$. This proposed mechanism does not align with what is observed in the TGOs of this study, as TiO_2 is not believed to solely exist at the alloy/oxide interface due to compositional differences observed in the backscattered micrographs of the interface (Figure 7). However, it is accepted that $TiNb_2O_7$ grows from the Nb-rich phase in the phase separated alloy, as the TGOs mimic the microstructures of the alloys investigated here. Future work will be conducted to elucidate whether $TiNb_2O_7$ forms from Nb exceeding its solubility limit in TiO_2, or if it forms from a reaction between $TiO_2 + Nb_2O_5$, as proposed by Cornie and Goodspeed[16].

4.2 Oxygen Diffusion Coefficients of $CrTaO_4$

Due to the shallow depth of the ^{18}O profiles in both tracer diffusion samples measured in this study, uncertainty is expected to be associated with each determined D_b. The cause of this shallow depth is likely due to the short $^{18}O_2$ exposure times and slow ^{18}O surface exchange rather than an insufficient amount of ^{18}O within the capsule during exposures. To address this, future $^{18}O_2$ exposure times for $CrTaO_4$ will be conducted on the time scale of days rather than hours.

In previous studies, $CrTaO_4$ has been proposed to be a protective oxide[20], where the growth rate of $CrTaO_4$ was measured to be intermediate to that of Al_2O_3 and Cr_2O_3[20]. The determined oxygen self-diffusion coefficients of $CrTaO_4$ from this work suggest that $CrTaO_4$ has similar coefficients to those of single crystal Cr_2O_3 and polycrystalline Al_2O_3, two of the most protective oxides (Figure 8). It should also be noted that the growth of Cr_2O_3 is not controlled by the diffusion of O, but rather that of Cr, which is three orders of magnitude faster than O diffusion in $CrTaO_4$ at 1200°C (Figure 8). This indicates that $CrTaO_4$ has the potential to be used as a protective oxide in refractory systems.

5. Conclusions

From this study, four main conclusions can be drawn:

1. Thermodynamic modeling does not accurately predict the oxide scale constitution of the Ti-Nb-TiO_2-$TiNb_2O_7$ system, indicating that kinetics likely plays a more significant role in the oxidation of Ti-Nb alloys.
2. Oxidation of Ti-Nb increases with Nb and $TiNb_2O_7$ content until a critical Nb concentration is reached, where the oxidation then decreases and $Ti_2Nb_{10}O_{29}$ preferentially forms relative to TiO_2.
3. An inhomogeneous oxide distribution occurs in the $TiO_2 + TiNb_2O_7$ oxide forming scales. It is proposed that $TiNb_2O_7$ grows directly from the Nb-rich phase formed by phase separation of the alloy during oxidation.
4. Preliminary results suggest that $CrTaO_4$ has similar oxygen self-diffusion coefficients to those of polycrystalline Al_2O_3 and single crystal Cr_2O_3 at 1200°C.

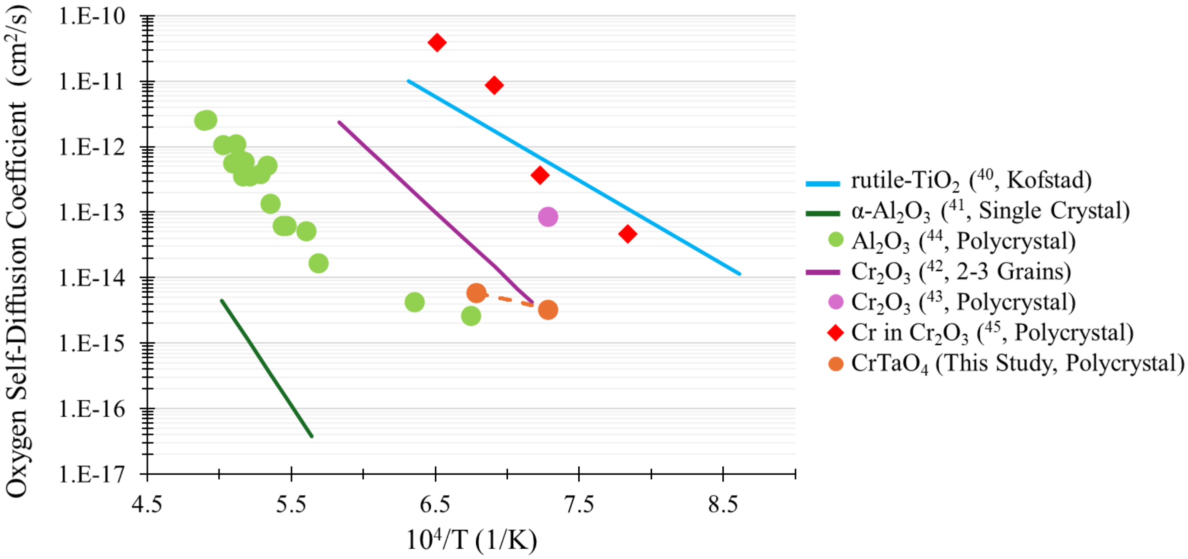

Figure 8. *Intrinsic oxygen self-diffusion coefficients of rutile-*TiO_2[40]*, single crystal*[41,42] *and polycrystalline*[43,44] Al_2O_3 *and* Cr_2O_3*, and Cr in polycrystalline* Cr_2O_3[45]*.* $CrTaO_4$ *is observed to have an oxygen diffusion coefficient similar to that of polycrystalline* Al_2O_3 *and single crystal* Cr_2O_3*.*

6. Acknowledgements

This work is funded by the U.S. Office of Naval Research, Grant number # N00014-23-1-2605: Complex Oxides for Improved Oxidation Resistance of Refractory Multiple Principal Element Alloys.

The author would like to thank: the Opila Research Group at UVA for their continued help and support throughout this research; Dr. Chuanzhen Zhou at North Carolina State University Analyzation Instrumentation Facility (NCSU AIF) for her ToF-SIMS measurements presented in this work; and Peter Connors at UVA for his assistance in arc-melting the tested alloys.

The XRD and SEM-EDS analysis done in this work was made possible through the University of Virginia Nanoscale Materials Characterization Facility (NMCF).

The author would also like to thank the Achievement Rewards for College Scientists – Metro Washington Chapter (ARCS MWC), specifically the JCM Foundation for their funding throughout this work, as well as the Virginia Space Grant Consortium (VSGC) Graduate Student Fellowship Program.

References

1. Wadsworth J, Nieh TG, Stephens JJ. Recent advances in aerospace refractory metal alloys. *International materials reviews*. 1988;33(1):131-150.
2. Anton DL, Snow DB, Giamei AF. Dispersion Strengthening of High Temperature Niobium Alloys. *Advanced Materials and Processing Techniques for Structural Applications; Paris; France; 7-9 Sept 1987*. Published online 1987:119-128.
3. Sankar M, Satya Prasad V V, Baligidad RG, Gokhale AA. Melting, Processing and Characterization of Nb-10W-2.5 Zr (Cb-752) Alloy. *Transactions of the Indian Institute of Metals*. 2017;70:1055-1062.
4. Wahl JB, Harris 3rd K. Improved 3rd Generation Single Crystal Superalloy CMSX-4® Plus (SLS)—A Study of Evolutionary Alloy Development. *Cannon-Muskegon: Muskegon, MI, USA*. Published online 1984.
5. Koff BL. Gas turbine technology evolution: A designers perspective. *J Propuls Power*. 2004;20(4):577-595.
6. ARPA-E. Ultrahigh Temperature Impervious Materials Advancing Turbine Efficiency. 2020.
7. Perepezko JH. The hotter the engine, the better. *Science (1979)*. 2009;326(5956):1068-1069.
8. Philips NR, Carl M, Cunningham NJ. New opportunities in refractory alloys. *Metallurgical and Materials Transactions A*. 2020;51(7):3299-3310.
9. Xiong W, Guo AXY, Zhan S, Liu CT, Cao SC. Refractory high-entropy alloys: A focused review of preparation methods and properties. *J Mater Sci Technol*. 2023;142:196-215.
10. Hebda J, Chang W. Niobium alloys and high temperature applications. In: *Niobium Science & Technology: Proceedings of the International Symposium Niobium*. Vol 2001. 2001.
11. E. Opila. *Pure Metals Group IV V, High Temperature Oxidation, Experimental Work Completed by K. D. Ardrey*. 2023.
12. Kofstad P, Steidel CA. High temperature oxidation of metals. *J Electrochem Soc*. 1967;114(7):167C.
13. Marnoch K. High-temperature oxidation-resistant hafnium-tantalum alloys. *JOM*. 1965;17(11):1225-1231.
14. Perepezko JH. *New Oxide Materials for an Ultra High Temperature Environment*. Univ. of Wisconsin, Madison, WI (United States); 2017.
15. Wang Y, Zhang B, Zhang C, Yin J, Reece MJ. Ablation behaviour of (Hf-Ta-Zr-Nb) C high entropy carbide ceramic at temperatures above 2100° C. *J Mater Sci Technol*. 2022;113:40-47.
16. Cornie JA, Goodspeed RC. *Development of Ductile Oxidation Resistant Columbium Alloy.* 1969.
17. Zhang P, Li Y, Chen Z, Zhang J, Shen B. Oxidation response of a vacuum arc melted NbZrTiCrAl refractory high entropy alloy at 800–1200 °C. *Vacuum*. 2019;162:20-27. doi:https://doi.org/10.1016/j.vacuum.2019.01.026
18. Butler TM, Chaput KJ, Dietrich JR, Senkov ON. High temperature oxidation behaviors of equimolar NbTiZrV and NbTiZrCr refractory complex concentrated alloys (RCCAs). *J Alloys Compd*. 2017;729:1004-1019.
19. Müller F, Gorr B, Christ HJ, et al. On the oxidation mechanism of refractory high entropy alloys. *Corros Sci*. 2019;159:108161.
20. Gorr B, Müller F, Schellert S, et al. A new strategy to intrinsically protect refractory metal

based alloys at ultra high temperatures. *Corros Sci*. 2020;166:108475.

21. Anber EA, Beaudry D, Brandenburg C, et al. Oxidation resistance of Al-containing refractory high-entropy alloys. *Scr Mater*. 2024;244:115997. doi:https://doi.org/10.1016/j.scriptamat.2024.115997
22. Schneider CA, Rasband WS, Eliceiri KW. NIH Image to ImageJ: 25 years of image analysis. *Nat Methods*. 2012;9(7):671-675. doi:10.1038/nmeth.2089
23. Toby BH, Von Dreele RB. GSAS-II: the genesis of a modern open-source all purpose crystallography software package. *Applied Crystallography*. 2013;46(2):544-549.
24. Degen T, Sadki M, Bron E, König U, Nénert G. The Highscore suite. *Powder Diffr*. 2014;29(S2):S13-S18.
25. Black DR, Mendenhall MH, Brown CM, Henins A, Filliben J, Cline JP. Certification of Standard Reference Material 660c for powder diffraction. *Powder Diffr*. 2020;35(1):17-22.
26. Kabekkodu SN, Dosen A, Blanton TN. PDF-5+: a comprehensive Powder Diffraction File^{TM} for materials characterization. *Powder Diffr*. 2024;39(2):47-59. doi:DOI: 10.1017/S0885715624000150
27. Perfler L, Kahlenberg V, Wikete C, Schmidmair D, Tribus M, Kaindl R. Nanoindentation, high-temperature behavior, and crystallographic/spectroscopic characterization of the high-refractive-index materials TiTa2O7 and TiNb2O7. *Inorg Chem*. 2015;54(14):6836-6848.
28. Gaskell DR, Laughlin DE. *Introduction to the Thermodynamics of Materials*. CRC press; 2024.
29. Backman L, Gild J, Luo J, Opila EJ. Part I: Theoretical predictions of preferential oxidation in refractory high entropy materials. *Acta Mater*. 2020;197:20-27. doi:https://doi.org/10.1016/j.actamat.2020.07.003
30. Fedorov NF, Mel'nikova O V, Saltykova VA, Pivovarova AP, Dib M, Strakhov VI. Nb2O5-TiO2 system study. Published online 1989.
31. Bale CW, Bélisle E, Chartrand P, et al. FactSage thermochemical software and databases, 2010–2016. *Calphad*. 2016;54:35-53. doi:https://doi.org/10.1016/j.calphad.2016.05.002
32. Andersson JO, Helander T, Höglund L, Shi P, Sundman B. Thermo-Calc & DICTRA, computational tools for materials science. *Calphad*. 2002;26(2):273-312. doi:https://doi.org/10.1016/S0364-5916(02)00037-8
33. Developed by Subcommittee: B09.04. ASTM B962-17 Standard Test Methods for Density of Compacted or Sintered Powder Metallurgy (PM) Products Using Archimedes' Principle. In: *Book of Standards Volume*. Vol 2. 5th ed. 2017.
34. Crank J. *The Mathematics of Diffusion*. Oxford university press; 1979.
35. S.J. Cooper. *Quantifying the Transport Properties of Solid Oxide Fuel Cell Electrodes*. Imperial College London; 2016.
36. Ogawa Y, Miura-Fujiwara E. Effect of Nb Addition on Oxide Formation on Ti–xNb Alloys. *Mater Trans*. 2019;60(10):2204-2212.
37. Gibbs GB, Graham D, Tomlin DH. Diffusion in titanium and titanium—niobium alloys. *Philosophical Magazine*. 1963;8(92):1269-1282.
38. Bakker H. Self diffusion in homogeneous binary alloys and intermediate phases. In: *Landolt-Börnstein-Group III Condensed Matter 26 (Diffusion in Solid Metals and Alloys)*. Springer-Verlag Berlin Heidelberg; 1990.
39. Miura-Fujiwara E, Ogawa Y, Niinomi M, Yamasaki T. Effect of Nb addition on high-temperature oxidation behavior, oxide layer structure, and its exfoliation resistance of Ti-Nb Alloys. In: *MATEC Web of Conferences*. Vol 321. EDP Sciences; 2020:05018.
40. Kofstad P. Defects and transport properties of metal oxides. *Oxidation of metals*. 1995;44(1):3-27.
41. Prot D, Monty C. Self-diffusion in α–Al2O3. II. Oxygen diffusion in 'undoped'single crystals. *Philosophical Magazine A*. 1996;73(4):899-917.
42. Hagel WC. Anion diffusion in α-Cr2O3. *Journal of the American Ceramic Society*. 1965;48(2):70-75.
43. King WE, Park JH. Anion Grain Boundary Diffusion in Cr2O3 and Cr2 O3-0.09 Weight Percent Y2O3. *MRS Online Proceedings Library (OPL)*. 1988;122:193.
44. Oishi Y, Kingery WD. Self-diffusion of oxygen in single crystal and polycrystalline aluminum oxide. *J Chem Phys*. 1960;33(2):480-486.
45. Lindner R, Åkerström Å. Selbstdiffusion und Reaktion in Oxyd-und Spinellsystemen. *Zeitschrift für Physikalische Chemie*. 1956;6(3_4):162-177.